

RESEARCH

Open Access



Lumped parameter simulations of cervical lymphatic vessels: dynamics of murine cerebrospinal fluid efflux from the skull

Daehyun Kim¹ and Jeffrey Tithof^{1*}

Abstract

Background Growing evidence suggests that for rodents, a substantial fraction of cerebrospinal fluid (CSF) drains by crossing the cribriform plate into the nasopharyngeal lymphatics, eventually reaching the cervical lymphatic vessels (CLVs). Disruption of this drainage pathway is associated with various neurological disorders.

Methods We employ a lumped parameter method to numerically model CSF drainage across the cribriform plate to CLVs. Our model uses intracranial pressure as an inlet pressure and central venous blood pressure as an outlet pressure. The model incorporates initial lymphatic vessels (modeling those in the nasal region) that absorb the CSF and collecting lymphatic vessels (modeling CLVs) to transport the CSF against an adverse pressure gradient. To determine unknown parameters such as wall stiffness and valve properties, we utilize a Monte Carlo approach and validate our simulation against recent *in vivo* experimental measurements.

Results Our parameter analysis reveals the physical characteristics of CLVs. Our results suggest that the stiffness of the vessel wall and the closing state of the valve are crucial for maintaining the vessel size and volume flow rate observed *in vivo*. We find that a decreased contraction amplitude and frequency leads to a reduction in volume flow rate, and we test the effects of varying the different pressures acting on the CLVs. Finally, we provide evidence that branching of initial lymphatic vessels may deviate from Murray's law to reduce sensitivity to elevated intracranial pressure.

Conclusions This is the first numerical study of CSF drainage through CLVs. Our comprehensive parameter analysis offers guidance for future numerical modeling of CLVs. This study also provides a foundation for understanding physiology of CSF drainage, helping guide future experimental studies aimed at identifying causal mechanisms of reduction in CLV transport and potential therapeutic approaches to enhance flow.

Keywords Cervical lymphatic vessels, Lymphatic system, Cerebrospinal fluid, Traumatic brain injury

Background

Cerebrospinal fluid (CSF) is a clear and colorless fluid that circulates around the brain and spinal cord, offering physical protection, acting as a “water cushion” to

the central nervous system [1]. Additionally, it serves as a medium for supplying nutrients to the brain [2]. Beyond these traditional functions, CSF has gained recognition for its potential role in clearing metabolic wastes from the brain [3]. The discovery of meningeal lymphatic vessels [4], which permeate nearly the entire meninges (the layers of tissue surrounding the brain) in mammals, has significantly advanced research on CSF and its flow, potentially linked to various neurological disorders.

*Correspondence:

Jeffrey Tithof
tithof@umn.edu

¹ Department of Mechanical Engineering, University of Minnesota, 111 Church St SE, Minneapolis, MN 55455, USA



© The Author(s) 2024. **Open Access** This article is licensed under a Creative Commons Attribution-NonCommercial-NoDerivatives 4.0 International License, which permits any non-commercial use, sharing, distribution and reproduction in any medium or format, as long as you give appropriate credit to the original author(s) and the source, provide a link to the Creative Commons licence, and indicate if you modified the licensed material. You do not have permission under this licence to share adapted material derived from this article or parts of it. The images or other third party material in this article are included in the article's Creative Commons licence, unless indicated otherwise in a credit line to the material. If material is not included in the article's Creative Commons licence and your intended use is not permitted by statutory regulation or exceeds the permitted use, you will need to obtain permission directly from the copyright holder. To view a copy of this licence, visit <http://creativecommons.org/licenses/by-nc-nd/4.0/>.

CSF is secreted from various sources, including the choroid plexus, ependymal cells, limited trans-capillary fluid flux, and metabolic water production [5]. Among these sites, the choroid plexus (found within the ventricles of the brain) is the main source, accounting for about 80% of CSF production. Following its production, CSF traverses the intricate ventricular system and subsequently reaches the subarachnoid space (SAS) surrounding the brain and spinal cord. Traditionally, the prevailing belief was that CSF is absorbed by arachnoid granulations. However, advancements in experimental techniques have revealed that substantial CSF also drains from the skull to eventually reach the cervical lymphatic vessels (CLVs) [6–11]. The contents of the CLVs may not be solely composed of CSF. The exact contribution of CSF to the total fluid within the CLVs is not fully understood and may vary under different conditions. However, it has been confirmed that fluid in the CLVs directly drains CSF, as microspheres injected into the cisterna magna of mice reach the CLVs within minutes [12].

The specific details of the route through which CSF reaches the CLVs are currently an area of active research and debate [13]. In animal studies, outflow along the cranial nerves, including the olfactory, optical, and facial nerves, as well as outflow to the meningeal lymphatic vessels and delivery to the deep cervical lymphatic nodes, has been well described. Compared to animal experiments, the understanding of CSF outflow pathways in humans is quite limited. Some evidence suggests that CSF outflow pathways exist through nasal lymphatics and meningeal lymphatic vessels [14, 15]. Several prior experiments in mice—especially of relevance for this study—suggest that a substantial fraction of fluid follows a pathway through the cribriform plate along the cranial nerves, draining into lymphatic vessels that eventually reach the CLVs [10, 12, 16–18].

Understanding fundamental aspects of CSF drainage to CLVs is significant due to its intricate association with various neurological disorders [19, 20]. Traumatic brain injury (TBI) also has been linked to CSF drainage disruption. In mouse models of TBI, research has revealed a significant reduction in CSF drainage through meningeal lymphatic vessels due to increased intracranial pressure (ICP) [21]. Additionally, it has been demonstrated that CSF flow serves as a conduit for transporting biomarkers associated with neurodegenerative diseases into the bloodstream via the cervical lymphatics [22]. More recently, TBI was linked to weakening of CLV activity and exacerbation of brain edema, which the authors argued arose as a consequence of a post-TBI surge in norepinephrine [12]. Notably, administration of a norepinephrine antagonist cocktail led to restoration of CLV function, reduction of edema, and improved cognitive

outcomes. These findings suggest TBI may directly impact CLV function, disrupting CSF drainage from the skull.

Despite the significant implications for advancing disease treatments, precise quantification of CSF drainage routes has proven challenging. Spatial and temporal limitations in imaging pose one of the biggest challenges. Since lymphatic vessels are narrow and long, and traverse a substantial fraction of the body that can be difficult to optically access [23, 24], *in vivo* visualization of a large fraction of the lymphatic network that drains CSF is tremendously challenging. Moreover, the alteration of biological variables, such as ICP, during experimental testing has the potential to disrupt this delicate biological system [25]. As a consequence, these inherent constraints in experiments leave many open questions which can perhaps be addressed via numerical simulation.

Numerical simulations serve as efficient, safe, and ethically desirable alternatives to experiments; simulations also enable manipulation of parameters and the ability to prescribe/determine precise conditions that may be difficult or impossible to achieve experimentally, such as pressures inside vessels. Numerous prior studies have used a numerical approach to model lymphatic vessels. Reddy et al. pioneered this field by creating the initial mathematical model for branching lymphatic vessels [26]. Their one-dimensional (1D) model simulated laminar lymphatic flow throughout the entire body, from the periphery through the main lymphatic system into the venous blood system. Their governing equation was based on the Navier-Stokes equation (in a 1D form) coupled with a thin-wall tube model. Quick et al. employed a circuit-theory approach, commonly employed in the simulation of cardiovascular systems [27], to simulate both individual lymphangions and a chain of lymphangions. Bertram et al. extended this methodology and focused on a series of lymphangions, highlighting the efficiency of sequential contractions compared to synchronized contractions for fluid transport [28]. These foundational models lay the groundwork for simulating a large number of interconnected lymphangions, with incorporation of compliant walls and valves. Notably, these models were primarily based on parameters from the thoracic duct and mesenteric lymphatic vessels.

In parallel, two-dimensional (2D) or three-dimensional (3D) models have typically focused on a single lymphangion and often utilize fluid-structure interaction techniques [29–31]. Such studies have investigated the influence of active contractions driven by nitric oxide and calcium ions on fluid drainage. Validation of Poiseuille flow under substantial radial contractions was also studied. Computational cost has largely confined such studies to simulation of a single lymphangion, although

some 2D/3D simulations for a series of lymphatic vessels, leveraging fluid-structure interaction approaches, have been achieved [32–34]. These studies tackled a range of factors, including the chain's length and its influence on mean flow rates, the effects of adverse pressure differences on flow rates, contraction timing, dynamics related to valve geometry impacting backflow, and the effects of valve elasticity. Again, it is worth highlighting that these simulations were based on lymphatic vessels in the other regions, such as mesenteric lymphatic vessels, and were not specifically tailored to CSF drainage through CLVs.

Currently, there is an absence of numerical models that predict fluid transport through CLVs. The goal of this study is to construct a comprehensive lumped parameter model that captures the intricate CSF drainage process in mice. In the absence of knowledge of the exact geometry and physical properties of CLVs, we use a Monte Carlo approach to identify a parameter regime that matches closely with experimental data. Simultaneously, we perform a parameter sensitivity analysis to examine the characteristics of CLVs and how changes in these parameters affect the CLV diameter and net volume flow rate. Using our model, we explore strategies to enhance CSF flow rate through CLVs by manipulating certain variables. Finally, we explore how the variation of ICP affects CSF efflux through the CLVs. This study is the first numerical model of CSF outflow through CLVs, providing novel insights into potential strategies to enhance CSF drainage. These findings provide guidance for future experimental research and serve as a valuable resource for optimizing CSF drainage strategies.

Methods

We use the lumped parameter method to model the nasal and cervical lymphatic system, which are treated as initial and collecting lymphatics. The versatility and computational efficiency makes this approach suitable for simulating the complexities and capturing the impact of uncertainties associated with this lymphatic network that connects the SAS to the end of the CLVs. Given the lack of detailed parameter values for CLVs in the literature (e.g., stiffness of the vessel wall, active tension due to smooth muscle cells, valve properties), this approach allows for computationally-efficient iterative determination of parameters to obtain agreement with experimental observations.

Modeling CSF drainage via CLVs

Lymphatic vessels typically consist of initial lymphatic vessels (lymphatic capillaries) and collecting lymphatic vessels [35]; in this study, CLVs are considered the only collecting lymphatic vessels. The initial lymphatic vessels form the starting point of the lymphatic system and

are responsible for absorbing ISF. These vessels consist of a single layer of endothelial cells, and their button-like junctions structure allows ISF and small particles to enter. As these interstitial lymphatic vessels merge, they give rise to larger lymphatic vessels known as collecting lymphatic vessels. Collecting lymphatic vessels consist of interconnected compartments called lymphangions which serve as the primary transporters of lymph within the lymphatic system. Unlike initial lymphatic vessels, collecting lymphatic vessels are covered by smooth muscle cells. There are two types of pumping mechanism in the collecting lymphatic vessels: extrinsic and intrinsic. Extrinsic pumping primarily occurs due to external forces acting on the lymphatic system. These external forces include skeletal muscle contractions, external compression from the pulsation of nearby arteries, and/or movement caused by respiration. Intrinsic pumping refers to the transport arising from natural contractile activity of smooth muscle cells lining the basement membrane of lymphatic vessels. In the periphery, a combination of extrinsic and intrinsic forces facilitate the movement of lymph against an adverse pressure gradient. The presence of valves between lymphangions ensures net transport of lymph by preventing backflow. Thus intrinsic and extrinsic pumping enables collecting lymphatic vessels to efficiently transport lymph to lymph nodes.

We used this general lymphatic structure to model CSF outflow through CLVs. A schematic of the model is illustrated in Fig. 1A. Due to limited anatomical data and flow measurements for humans, we instead developed our model to capture murine anatomy. Even though the exact route connecting the CSF in SAS to the lymphatic capillaries is not fully established [13], recent experiments suggest that tiny lymphatics have direct connection to the SAS across the cribriform plate [16, 36–38]. Based on these findings, we assume there are direct connections through which the lymphatic capillaries absorb CSF from the SAS. These capillaries then merge to form larger vessels, with diameters prescribed by Murray's Law but with a different exponent value ($n = 1.45$) [39]. For simplicity, we assume that initial lymphatics are impermeable and absorption of CSF occurs at the tip of the vessels. CSF in the initial lymphatics is transported to the CLVs, then eventually pumped to the central venous blood. Fig. 1B summarizes the mathematical model that describes CSF efflux from the SAS to CLVs then venous blood. Our model is based on the lumped parameter method, which involves constructing a hydraulic network that is analogous to an electrical circuit, so our simulation diagram includes circuit elements; the equivalent resistor $R_{initial}$, for example, captures the hydraulic resistance of the initial lymphatic vessels.

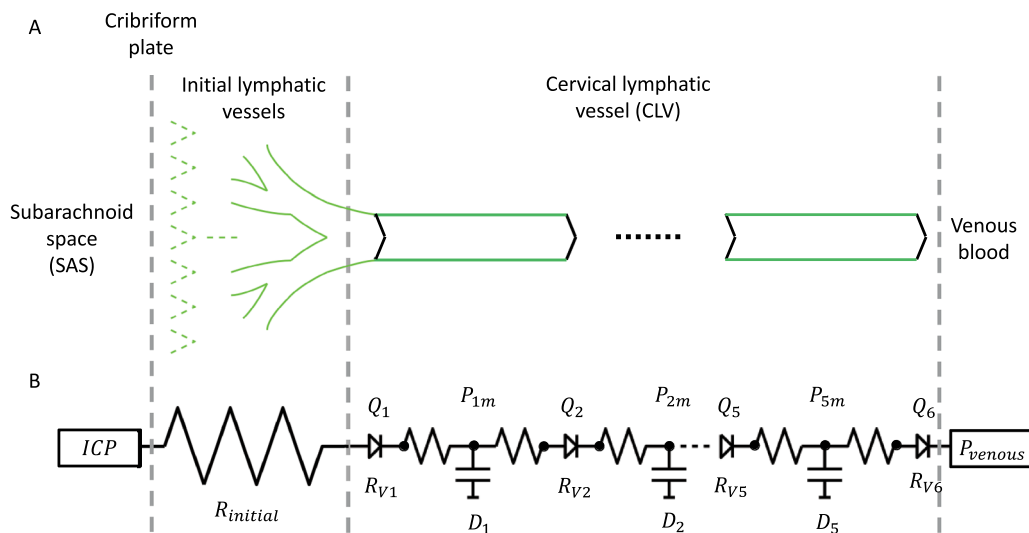


Fig. 1 Comparative illustration and mathematical approach to modeling CSF drainage. (A) Illustration of the biological pathway for CSF drainage through CLVs. CSF in the SAS is directly absorbed by lymphatic capillaries that cross the cribriform plate. These capillaries merge to form larger vessels, which eventually connect to the CLVs. The CLVs then transport the CSF back into the central venous blood. (B) Schematic of the mathematical model of this CSF drainage pathway. The inlet pressure is the ICP, and the lymphatic capillaries are modeled using a net equivalent hydraulic resistance ($R_{initial}$). The outlet pressure is equal to that of central venous blood. CLVs are modeled to incorporate contractions and expansions of lymphangions, as well as opening and closing of valves in between. Hydraulic resistance of the valves (R_V) are represented as diodes in the schematic. Each lymphangion has the same length (L) and its own diameter (D). While capacitance is not explicitly included in our governing equations, the change in vessel diameter serves a capacitance-like function and is therefore denoted with a capacitance symbol. The pressures within each lymphangion are calculated at three points: just past the inlet, the midpoint, and just before the outlet. The inlet and outlet pressures are used to calculate the volume flow rates (Q) at the valves. The pressures at the midpoint (P_m) are determined using the transmural pressure equation. The design of the CLV part is inspired by Bertram et al. [28]

The size of the initial lymphatics located near the cribriform plate was estimated by analyzing images from Spera et al. [18] (tip diameter: $7.5 \mu\text{m}$) and Norwood et al. [16] (length of total branches: $370 \mu\text{m}$). By applying the modified Murray's Law ($d_i^{1.45} = d_{i+1}^{1.45} + d_{i+1}^{1.45}$), we calculated the diameters of parent vessels and number of branching generations until their diameter reached the median diameter of CLVs ($D_0 = 84.1 \mu\text{m}$) as reported in Hussain et al. [12]. We assume that the tip of two daughter branches of the lymphatic capillaries with the same diameter merge into one parent vessel. Eventually, the merged parent vessels join to form the first lymphangion of the collecting lymphatic vessels. We obtained $N = 5$ for the number of generations (compared to $N = 11$ for standard Murray's law with exponent 3). The modified exponent in our model results in a smaller number of generations ($N = 5$), leading to smaller diameters of the branches. Also, each branch becomes longer, as the total length of the entire branching structure is fixed. Subsequently, we computed the hydraulic resistance of this branching network under the assumption of Hagen-Poiseuille flow. Finally, the total hydraulic resistance was calculated using computation of a series of parallel resistances as,

$$R_{initial} = \sum_{i=1}^N \frac{128\mu l / \pi d_i^4}{2^i} = 2.64 \times 10^9 \text{ dyne s/mL cm}^2 \tag{1}$$

where i is the specific generation, μ is dynamic viscosity of the CSF, l is length of each segment of daughter capillaries, and d_i is the initial lymphatic vessel diameter at generation i . Note that lower case d and l are used to represent the initial lymphatic vessels, while upper case D and L are used to represent the collecting lymphatic vessels.

Bertram et al's works are the inspiration for our approach to modeling CLVs [28, 40, 41]. We assume a collecting lymphatic vessel consists of five lymphangions, based on our estimates of 10 mm from the nasal mucosa to superficial cervical lymph node and a 2 mm lymphangion length [12, 17]. Each lymphangion, j , is characterized by time-dependent variables, namely, CLV diameter D_j , and pressures $P_{j,1}$, $P_{j,m}$, and $P_{j,2}$ representing the pressures just after the inlet, at the midpoint, and just before the outlet, respectively. Note that the use of three points per lymphangion (rather than just one) enables more realistic modeling that can capture valve prolapse [42]. Additionally, the model includes the volume flow rates

Q_j and Q_{j+1} , representing the inflow and outflow rates at each valve of a given lymphangion, respectively. The fluid flow from one chamber to the next chamber is described by a control volume discretization of the equations governing conservation of mass and momentum [28, 40, 42],

$$\frac{dD_j(t)}{dt} = \frac{2(Q_j(t) - Q_{j+1}(t))}{\pi L D_j(t)} \tag{2}$$

$$\frac{P_{j,1}(t) - P_{j,m}(t)}{L} = \frac{64\mu Q_j(t)}{\pi D_j(t)^4}, \quad \frac{P_{j,m}(t) - P_{j,2}(t)}{L} = \frac{64\mu Q_{j+1}(t)}{\pi D_j(t)^4} \tag{3}$$

under the quasi-steady assumption of fully developed Hagen-Poiseuille flow. This assumption is justified by the small Reynolds number ($Re = UD_0/\nu \approx 7 \times 10^{-3}$) and small Womersley number ($Wo = D_0\sqrt{2\pi f}/\nu \approx 0.05$) of flow in the CLVs, where $U = 64.8 \mu\text{m/s}$ is the mean flow speed, $D_0 = 84.1 \mu\text{m}$ is the mean CLV diameter, $\nu = 0.7 \times 10^{-6} \text{m}^2/\text{s}$, and $f \approx 0.04 \text{Hz}$ is the contraction frequency. Note that we provide derivations of equations (2-3) in Appendix A. Each lymphangion is separated by valves with hydraulic resistance [28],

$$R_{V_{j+1}}(t) = R_{V_{\min}} + R_{V_{\max}} \left(\frac{1}{1 + \exp(-s_{\text{open}}((P_{j,2}(t) - P_{j+1,1}(t)) - P_{\text{open}}))} \right), \tag{4}$$

where $R_{V_{\min}}$ and $R_{V_{\max}}$ are the respective minimum and maximum hydraulic resistance of the valves when open or closed, P_{open} is the minimum pressure required to open the valve, and s_{open} is the slope of the valve opening. A large s_{open} means a more rapid response of the valve opening to changes in pressure difference across the valve, while a smaller s_{open} indicates a more gradual response. The volume flow rate through the valves is calculated based on a momentum equation analogous to Ohm's law,

$$Q_{j+1}(t) = \frac{P_{j,2}(t) - P_{j+1,1}(t)}{R_{V_{j+1}}(t)}. \tag{5}$$

The associated sets of differential algebraic equations are then closed by specifying the transmural pressure (i.e., pressure difference between inside and outside the lymphangion) using an equation that contains both passive and periodic contractile components [28]:

$$P_{j,m}(t) - P_{\text{external}} = P_d \left(\exp\left(\frac{D_j(t)}{D_d}\right) - \left(\frac{D_d}{D_j(t)}\right)^3 \right) + \frac{M}{D_j(t)} (1 - \cos(2\pi f(t - t_{dj}))), \tag{6}$$

where P_{external} is a uniform pressure external to the lymphangions, P_d and D_d are passive properties that account for mechanical characteristics of a lymphangion's contractions and expansions, M is the active tension, and t_{dj} is temporal phase between contractions of adjacent lymphangions (these parameters are discussed in more detail below). We assume the external pressure P_{external} is constant and slightly lower than the inlet and outlet pressures to make the transmural pressure operate more dynamically, similar to Bertram et al's work [28].

Parameter estimation

We first discuss parameters in the equations that are well-known based on literature and experimental observations, which are detailed in Table 1. The frequency of lymphangions' contractions, f , and the length of each lymphangion, L , are determined directly from in vivo images [12] using our recently published image analysis techniques [43]. The dynamic viscosity of CSF was used in our model [44]. We used the same values for the temporal phase between adjacent lymphangion contractions, t_{dj} , and the slope of valve opening, s_{open} , as in previous

studies [28, 41].

Estimating other parameters poses a substantial challenge, particularly for those not directly measurable, such as properties of the cervical lymphatic vessel walls (P_d, D_d), active tension generated by smooth muscle cells (M), the minimum pressure required to open the valve (P_{open}), and hydraulic resistance of the valves ($R_{V_{\min}}, R_{V_{\max}}$). While more detailed explanation of these constants is available in the original works [28, 40, 41, 45], it is worthwhile to provide a brief explanation of these unknown properties here. P_d represents the vessel wall stiffness. A higher P_d value means that the transmural pressure reacts more sharply to any change in vessel diameter. D_d is the threshold diameter at which the vessel begins to experience positive or negative transmural pressure. When the lymphangion's diameter (D_j) surpasses D_d , the transmural pressure becomes positive, with the shape of an exponential curve. Conversely, when the lymphangion's diameter is less than D_d , the transmural pressure becomes negative, described by a cubic function. M represents the tension generated by smooth muscle cells around the vessel. The transmural pressure incorporates this active tension (M) as well as the vessel's passive properties (P_d and D_d) to account for the mechanical characteristics of a lymphangion's contractions and expansions. P_{open} is the threshold pressure for the opening of valves

Table 1 Reasonably well-known parameters for modeling CLVs, as used in this study

Parameters	Definitions	Value	Unit	Reference
f	Contraction frequency	2.4 (Default) 1–20 (Fig. 5B)	min^{-1}	[12]
L	Length of lymphangion	2	mm	[12]
n	Number of lymphangions	5		Assumed
t_d	Temporal phase adjacent lymphangion contractions	90	degree	[41]
s_{open}	Slope of valve opening	0.2	cm^2/dyne	[40]
μ	Dynamic viscosity of CSF	0.007	$\text{Pa} \cdot \text{s}$	[44]
$P_{external}$	External pressure	3.75 (Default) 2–4 (Fig. 5C)	mmHg	Assumed
ICP	Intracranial pressure	4 (Default) 10 (Elevated ICP for Fig. 6) 4–8.84 (Fig. 5D)	mmHg	[46, 47]
P_{venous}	Central venous pressure	6 (Default) 6–10.44 (Fig. 5D)	mmHg	[48]
$R_{initial}$	Equivalent hydraulic resistance of lymphatic capillaries	3.21×10^8 ($n = 3$) 2.65×10^9 ($n = 1.45$)	$\text{dyne} \cdot \text{s}/(\text{mL} \cdot \text{cm}^2)$	[39]

between adjacent lymphangions. The valves are analogous to a diode in an electrical circuit. When the pressure difference across the valve exceeds P_{open} , the resistance of the valve becomes approximately $R_{V_{min}}$. When the upstream pressure (pressure before the valve) is lower than the downstream pressure (pressure after the valve), the hydraulic resistance of the valve becomes approximately $R_{V_{max}}$, meaning that if this value is very large, the valve is practically closed.

To overcome the challenge of not knowing the mechanical properties of CLVs, we adopt an inverse problem-solving approach based on a Monte Carlo method in which we vary parameters then compare model outputs (diameter of the third lymphangion and volume flow rate through the downstream valve of the third lymphangion) to experimental measurements of the median vessel diameter (76 – 88 μm) and mean volume flow rate (0.012 – 0.034 $\mu\text{l}/\text{min}$) [12]. This approach allows us to iteratively adjust and optimize our parameters by validating outputs against experimental measurements, aiming to achieve a more accurate and comprehensive model of the CSF drainage dynamics.

We set bounds for unknown parameters based on prior research on rat mesenteric lymphatic vessels [28, 40, 41,

45, 49]. The lower and upper bounds we set come from the minimum and maximum of reported values. We then expanded the bounds by subtracting or adding twice the standard deviation σ . Our resulting bounds for unknown parameters are summarized in Table 2. We next generated a random uniform distribution for each of the unknown parameters in accordance with each range. 10,000 simulations were conducted based on these randomly sampled parameters, and results from the model were compared to the median diameter and mean volume flow rate of the CLVs as measured in vivo.

To run a given simulation, the diameters, pressures, and volume flow rates in the differential algebraic equations (1)-(3), coupled with valve and transmural pressure equations (4)-(6), were solved numerically. All the numerical code was written in Python, primarily using the Numpy and Scipy libraries [50, 51]. The Python scripts are available in the supplementary material.

Briefly, after defining parameters, time steps, and geometry, the code loops over time. The diameter was updated using the 4th order Runge-Kutta method, which utilizes SciPy library's 'fsolve' function to calculate the pressures at each lymphangion location based on an initial guess of the diameters. Using the updated

Table 2 Bounds on unknown parameters, used in our Monte Carlo approach to modeling CLVs to determine parameter sets that lead to simulations that closely match average experimental measurements

Parameters	Definitions	Lower Bound	Upper Bound	Unit
M	Active tension	3.6	24.3	dyne/cm
$R_{V_{min}}$	Minimum valve resistance	600	2.83×10^6	dyne · s/(mL · cm ²)
$R_{V_{max}}$	Maximum valve resistance	1.2×10^7	2.82×10^{10}	dyne · s/(mL · cm ²)
P_{open}	Valve opening pressure	- 70	- 15	dyne/cm ²
P_d	Constitutive-relation constant	20	732	dyne/cm ²
D_d	Constitutive-relation constant	0.00845	0.0613	cm

diameters and pressures, valve resistances (which require the pressure difference across the valves) were then determined. The volume flow rates through the valves were then computed using the pressure differences and valve resistances, thus evolving the system forward in time by one time step. The pressure was used to determine convergence (taking into account that it varies periodically). In each simulation, the number and timing of contractions were approximated based on the input contraction frequency. As the simulation progressed in time and surpassed each estimated contraction cycle, the code detected the local peak pressure within each cycle. If the difference between the current and previous peak pressure, as well as the difference between the previous two peak pressures, falls below the pressure tolerance value (1×10^{-5} mmHg), the simulation stops. The simulation would then output the pressures, diameters, and volume flow rates for the final three consecutive cycles.

When testing various combinations of parameters using a Monte Carlo approach, the median diameter ($med(D_{sim})$) and mean volume flow rate \bar{Q}_{sim} for each simulation were calculated to be compared with experimental data. If these values fell within the experimental ranges ($med(D_{exp})$ of 76 – 88 μm and \bar{Q}_{exp} of 0.012 – 0.034 $\mu\text{l}/\text{min}$) [12], we noted that particular parameter set. We continued this process for every randomly-chosen parameter set and repeated the same numerical procedure. A summary of our numerical approach, including the Monte Carlo parameter selection, is depicted in Fig. 2. Note that we stored the results of all simulations (including those that did not meet our criteria) for the sake of performing sensitivity analysis.

Results

We now present simulation results, which detail our parameter estimations, overall CSF efflux through lymphatic vessels, a sensitivity analysis of the parameters affecting CLVs, and the impact of branching in initial lymphatic vessels. It is important to note that the volume

flow rate is calculated at the valves, whereas the median diameters ($med(D_{sim})$) are calculated in the middle of each lymphangion. The mean volume flow rate \bar{Q}_{sim} used throughout the results refers to the time-averaged downstream volume flow rate of the third lymphangion in our simulation. Similarly, the reported median diameter is the temporal median of the third lymphangion diameter. Additionally, we restate the definition of each unknown parameter used in the Monte Carlo simulation, for convenience. P_d and D_d represent the properties of the CLV wall that control the stiffness of the vessel. M denotes the magnitude of active tension generated by smooth muscle cells. P_{open} is the minimum pressure required to open the valve. $R_{V_{min}}$ is the hydraulic resistance of the valves in their open state, whereas $R_{V_{max}}$ is the hydraulic resistance of the valves in their closed state.

Inverse problem: Monte Carlo approach

We conducted a Monte Carlo simulation to estimate parameters that are consistent with experimental observations. Out of 10,000 simulations, 3117 successfully converged. The converged simulations indicate that M , D_d , and P_d must fall within a narrow range for simulations to successfully converge. To further explore the sensitivity, we narrowed the values of M , D_d , and P_d and performed an additional 2000 simulations, randomly sampling parameters from within these revised limits (Fig. 3).

The parameter sensitivity analysis revealed that active tension (M) has a negative correlation with vessel diameter (Fig. 3A). Additionally, increasing M results in an increase in \bar{Q}_{sim} . Vessel wall stiffness (P_d) is weakly correlated with vessel diameter and weakly anti-correlated with \bar{Q}_{sim} (Fig. 3B). The threshold diameter (D_d) shows a linearly proportional relationship with $med(D_{sim})$ that becomes super-linear above about $D_d = 0.016$ cm; there is also a slight decreasing trend in \bar{Q}_{sim} for values of D_d exceeding about 0.014 cm (Fig. 3C). These findings suggest that the threshold diameter, active tension, and—to a lesser extent—vessel wall stiffness generated by smooth muscle cells significantly influences CLV diameter.

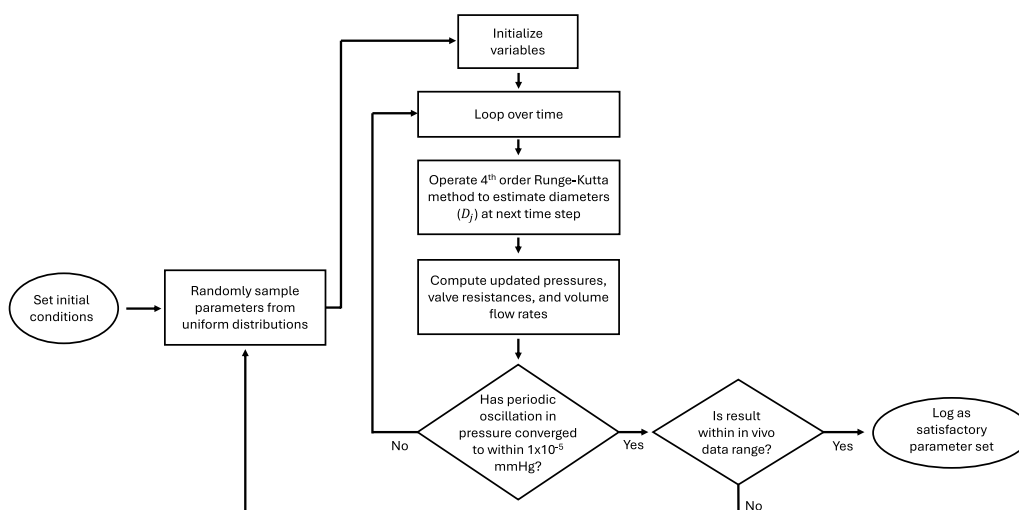


Fig. 2 A flow chart depicting the algorithm used in our Monte Carlo parameter search

P_{open} does not show a clear correlation with either $med(D_{sim})$ or \bar{Q}_{sim} (Fig. 3D). In contrast, R_{Vmax} shows a strong negative correlation with $med(D_{sim})$ and a positive correlation with \bar{Q}_{sim} , but only for small values of R_{Vmax} (Fig. 3E). Interestingly, when R_{Vmax} becomes too small, vessel size increases excessively, and \bar{Q}_{sim} turns negative, indicating that backflow exceeds forward flow. This suggests that the closure of the valve is crucial for prograde net transport, even more so than the pressure difference required to open the valve (for the parameter ranges considered here, anyway). R_{Vmin} does not exhibit a clear correlation with $med(D_{sim})$ (Fig. 3F). However, once $[R_{Vmin}]$ exceeds 0.8, \bar{Q}_{sim} begins to decrease. This suggests that the valve should open properly (reducing the resistance through it) to enhance the flow.

From this analysis, we identified the following parameters that lead to simulation results that align closely with experimental data: $M = 23.9$ dyne/cm, $R_{Vmin} = 1.89 \times 10^6$ dyne s/mL cm², $R_{Vmax} = 2.22 \times 10^{10}$ dyne s/mL cm², $P_{open} = -18.9$ dyne/cm², $P_d = 472$ dyne/cm², and $D_d = 1.63 \times 10^{-2}$ cm. This parameter set will be used below for further analysis. With the given parameter sets, $med(D_{sim})$ of the third lymphangion was 86.39 μ m and \bar{Q}_{sim} was 0.017 μ l/min.

CSF efflux through CLVs

The adverse pressure difference that CLVs must overcome is higher than other lymphatic regions. The CSF must be transported against this adverse pressure, and this is enabled through intrinsic pumping in the presence of bileaflet valves in the lymphangions. Fig. 4A–D illustrate this process. In Fig. 4A, the ICP is indicated by a red circle, while central venous blood pressure is represented by a cyan circle. The colors of the X symbols in Fig. 4A correspond to the locations of pressures (Fig. 4B) and diameters (Fig. 4C) for each lymphangion. The arrows in Fig. 4A represent the volume flow rate downstream from the X symbols, and these flow rates are plotted in Fig. 4D using the corresponding colors. It is worth noting that three pressures per lymphangion were calculated, but only the pressures in the middle of each lymphangion were plotted in Fig. 4B to avoid overcrowding. The three pressures computed for each lymphangion are not identical but are similar to each other.

We now examine the first (blue in Fig. 4A) and second (orange in Fig. 4A) lymphangions. At 160 s, the pressure in the first lymphangion is lower than the second lymphangion (Fig. 4B). As the pressure inside the first lymphangion begins to exceed that of the

(See figure on next page.)

Fig. 3 Results from the Monte Carlo search and analysis of parameter sensitivity. Median diameter ($med(D_{sim})$) or mean volume flow rate (\bar{Q}_{sim}) as a function of six different model parameters: **A** active tension, **B** vessel wall stiffness, **C** threshold diameter for positive or negative transmural pressure in the vessel, **D** threshold pressure to open the valve, **E** normalized hydraulic resistance of the closed valve, and **F** normalized hydraulic resistance of the open valve. Data points from individual simulations are shown as light gray scatter points. Mean values are plotted in solid blue for $med(D_{sim})$ and in solid orange for \bar{Q}_{sim} . Standard deviations are plotted in black, with the regions between them shaded in light blue or light orange. The hydraulic resistance of the valves, R_{Vmin} and R_{Vmax} are normalized by their maximum values such that $[R_{Vmin}] = R_{Vmin} / max(R_{Vmin})$ and $[R_{Vmax}] = R_{Vmax} / max(R_{Vmax})$ (see text for values). Note that the choice of y-axis limits excludes some outliers, but plots that include all data points are included in the supplementary materials (Fig. S1)

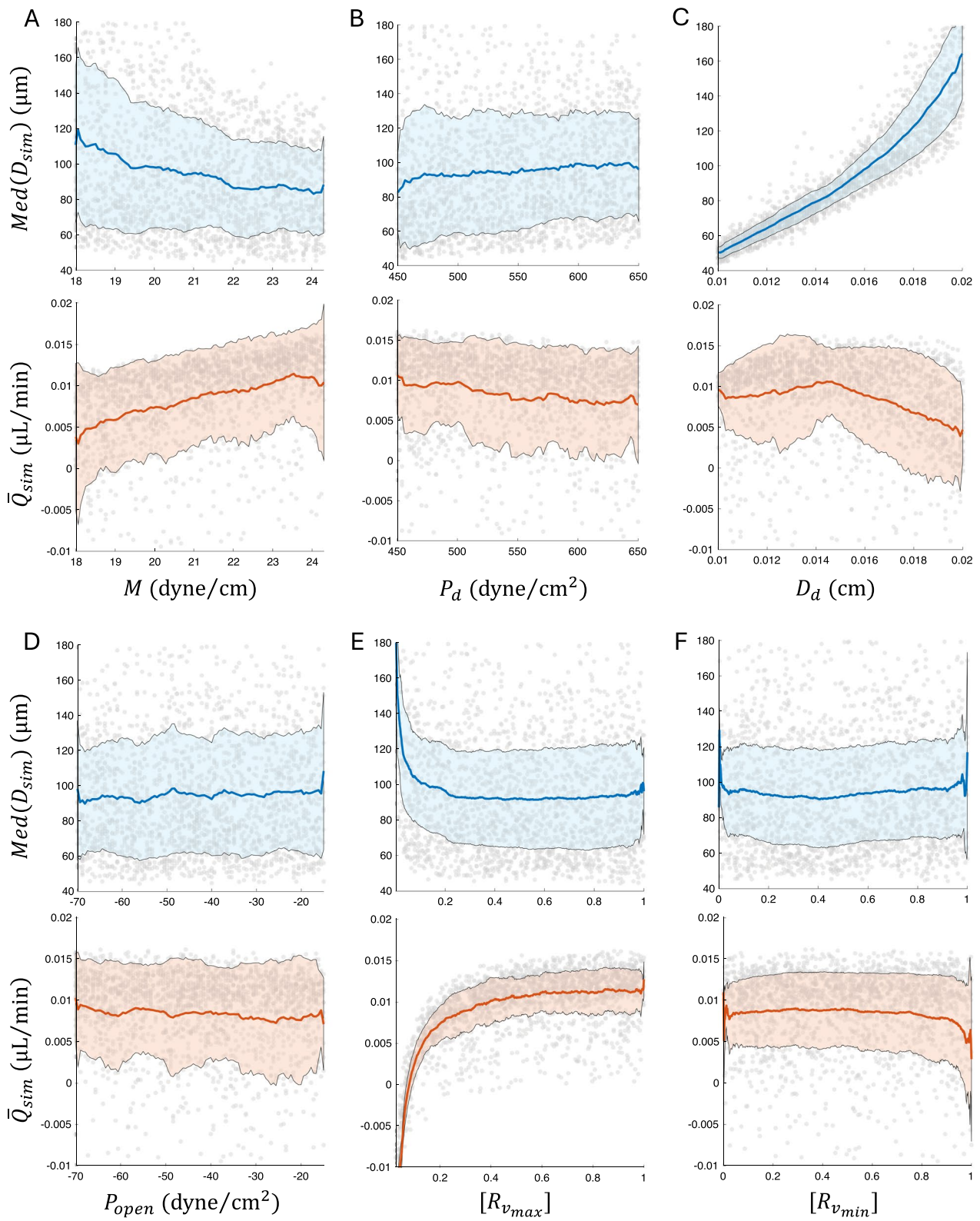


Fig. 3 (See legend on previous page.)

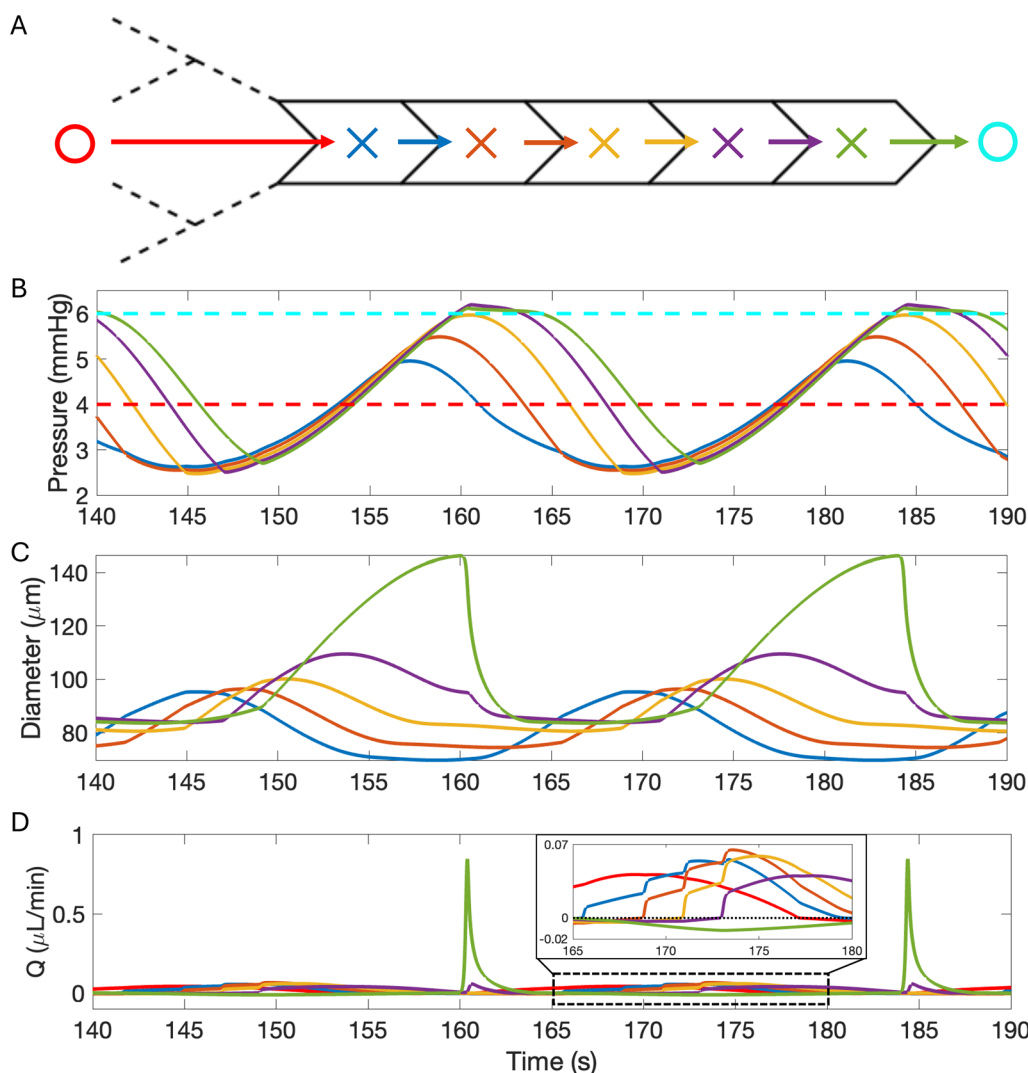


Fig. 4 CSF drainage through CLVs. **A** Illustration of the geometry of the simulation. A red and a cyan circle indicate the locations at which upstream pressure (ICP) and downstream pressure (venous blood pressure), respectively, are plotted in **(B)**. Additional X symbols inside each lymphangion are color-coded to indicate the locations of pressure and diameter in **(B)** and **(C)**; similarly, arrows inside each valve are color-coded to indicate volume flow rate plotted in **(D)**. **B** Plot of pressures in the middle of each lymphangion ($P_{j,m}$) versus time. We assume constant pressure for the inlet (red dashed line) and outlet (cyan dashed line). **C** Plot of diameters versus time. **D** Plot of volume flow rate versus time. Note the large green peak corresponds to flow through the last valve, furthest right in **(A)**. The subplot in **(D)** provides a magnified view of the volume flow rate plot for 165 – 180 s to better visualize the backflow

second lymphangion (Fig. 4B) and surpasses the additional threshold pressure needed to open the valve (P_{open}), CSF is transported from the first to the second lymphangion (Fig. 4D) as the first lymphangion contracts (Fig. 4C) and opens the valve between them. This results in the expansion of the second lymphangion as the CSF flows in. However, this forward flow is not continuous. The pressure in the second lymphangion exceeds that of the first lymphangion again (Fig. 4B), causing the valve between them to close, leading to a small but non-negligible backflow from the second to the first lymphangion

(subplot in Fig. 4D). The cycle of expansion and contraction of each lymphangion, driven by oscillatory active tension from smooth muscle cells (intrinsic pumping) and the opening and closing of the valves, enables CSF transport against a relatively large adverse pressure difference (~2 mmHg), ultimately facilitating fluid drainage into the central venous blood.

An interesting flow is observed at the inlet and outlet of the CLVs (Fig. 4D). The volume flow rate at the first valve is positive over a wide time span (red curve in Fig. 4D), due to the presence of large-resistance

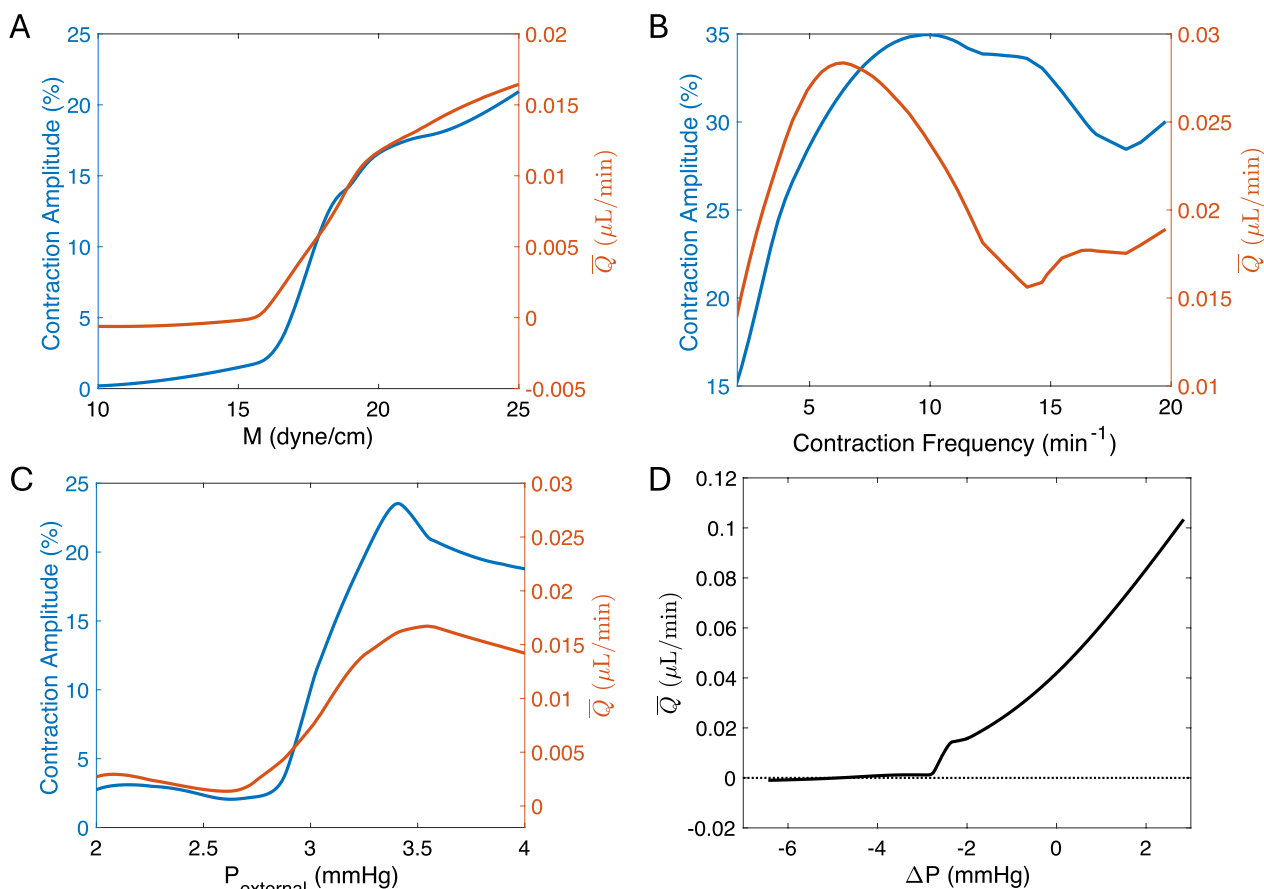


Fig. 5 Effects of varying active tension, contraction frequency, external pressure, and longitudinal pressure difference. These quantities are varied for all lymphangions in our model, but results are plotted for only the third lymphangion. **A** Contraction amplitude (left y-axis) and mean volume flow rate, \bar{Q} , (right y-axis) as a function of M (active tension of smooth muscle cells). **B** Contraction amplitude (left y-axis) and \bar{Q} (right y-axis) as a function of f (contraction frequency). **C** Contraction amplitude (left y-axis) and \bar{Q} (right y-axis) as a function of P_{external} (external pressure); the longitudinal pressure difference is fixed at $\Delta P = -2$ mmHg, where $\Delta P = \text{ICP} - P_{\text{venous}}$ (i.e., inlet pressure – outlet pressure). **D** \bar{Q} as a function of longitudinal pressure difference ΔP ; the external pressure is fixed at $P_{\text{external}} = 3.75$ mmHg

initial lymphatics attached to it. The addition of the net hydraulic resistance of the initial lymphatics results in a gradual change in the volume flow rate. The impact of the net hydraulic resistance of the initial lymphatic vessels will be discussed in more detail in the following section. The outflow from the last lymphangion to the central venous blood is narrow but high (green curve in Fig. 4D). This is due to the higher contraction amplitude of the last lymphangion compared to the other lymphangions. It is important to note that the time-averaged volume flow rate across all lymphangions remains consistent, in accordance with the mass conservation.

Effect of intrinsic pumping and variable pressures

Lymphatic vessels rely on both intrinsic and extrinsic pumping mechanisms to transport fluid. Active tension generated by smooth muscle cells in response to stimuli,

such as adrenergic and nitric oxide signals, is the primary driver of intrinsic pumping, regulating lymph flow. As active tension (M) increases, lymphangion contraction amplitude, which we define as the difference between the maximum and minimum diameter divided by the maximum diameter ($\frac{D_{\text{max}} - D_{\text{min}}}{D_{\text{max}}}$), also increases (blue curve in Fig. 5A). The orange curve in Fig. 5A illustrates the relationship between mean volume flow rate (\bar{Q}) and M , indicating that a higher value of M (i.e., higher contraction amplitude) results in greater net transport.

In Fig. 5A, two key points stand out. First, as M increases in the 10 – 16 dyne/cm range, the contraction amplitude increases slowly, and \bar{Q} remains nearly constant. This is because the active tension is too low to significantly affect contractions compared to the lymphangion’s passive properties. In the 16 – 20 range for M , the contraction amplitude increases dramatically

as active tension dominates the lymphangion's passive properties. Beyond $M \approx 21$, the increase in contraction amplitude slows down, suggesting \bar{Q} may stabilize beyond this point. This is because the vessel diameter remains small when active tension is large (and hydraulic resistance depends sensitively on diameter, scaling with D^4). This indicates that excessively high tension does not necessarily promote CSF transport, and the optimal range is likely around 20 – 24 dyne/cm.

Next, we fixed $M = 23.85$ dyne/cm and adjusted the contraction frequency, f , from 1 – 20 min^{-1} (Fig. 5B). Initially, both the contraction amplitude and \bar{Q} rose sharply for frequencies in the range of 1 – 6 min^{-1} . For frequencies between 6 and 10 min^{-1} , \bar{Q} decreases while the contraction amplitude continued to increase gradually. From 10 to 14 min^{-1} , \bar{Q} continues to decrease while contraction amplitude only decreases slightly. At a frequency of 14 min^{-1} , \bar{Q} reaches a local minimum. Beyond this point, \bar{Q} begins to increase slowly. This suggests that there is a wide range over which increases in contraction frequency coincide with increases in contraction amplitude, but maximum \bar{Q} occurs for frequencies close to 6 min^{-1} and decreases substantially for faster/slower contractions. At high contraction frequencies ($\gtrsim 10 \text{ min}^{-1}$), the lymphangion's contraction amplitude is likely reduced because it begins contracting before becoming fully inflated.

We also tested the effect of varying external pressure (Fig. 5C). When the external pressure is in the lower range (2 – 2.7) mmHg, the contraction amplitude of the vessels is low, resulting in a low \bar{Q} . For external pressures of about 2.7 – 3.4 mmHg, the contraction amplitude of the vessels increases, leading to a corresponding increase in \bar{Q} . However, once the external pressure exceeds about 3.4 mmHg, the contraction amplitude begins to decrease, causing a slight decrease in \bar{Q} . These results indicate that external pressure affects the intrinsic pumping of the CLVs, with an optimal range of external pressure necessary for effective pumping. At lower external pressures, the lymphangion is inflated with reduced contractility and thus \bar{Q} is low. Conversely, at higher external pressures, the diameter of the lymphangion is significantly reduced, but the substantial contraction amplitudes are able to maintain considerable \bar{Q} , at least for the range of external pressures we considered.

Finally, we tested different net pressure drops between the inlet and outlet in our model of the CSF outflow pathway (Fig. 5D). We varied both the ICP (inlet pressure) and P_{venous} (outlet pressure) to model outflow during various scenarios that affect pressure (e.g., different body postures, variable hydration states). From the ranges of ICP and P_{venous} listed in Table 1), we estimated the pressure

drop ($\Delta P = ICP - P_{\text{venous}}$) across the model to vary from –6.44 mmHg to 2.84 mmHg. For ΔP values between –6.44 mmHg and –2.9 mmHg, either the inlet pressure was too small or the outlet pressure was too high, resulting in an overall negative \bar{Q} or positive but negligible \bar{Q} . This indicates that for this range of pressure differences, the CLV pumping is not strong enough to transport fluid to the cervical lymph nodes and instead a small amount of fluid is transported retrograde. For ΔP values above –2.9 mmHg, a positive \bar{Q} with a gradually varying slope was observed.

Effect of lymphatic capillary branching assumptions

In our final test, we examined how lymphatic capillary branching affects net volume flow rate. We applied an inlet pressure corresponding to either normal ICP (4 mmHg) or elevated ICP (10 mmHg), as indicated in Fig. 6A. We then tested two different branching scenarios: one adhering to the typical Murray's law (with exponent 3) and another corresponding to Murray's law with exponent 1.45 [39]. The model with the smaller exponent led to smaller vessel diameters, but longer length, across each bifurcation compared to the normal case, ultimately generating a higher hydraulic resistance R_{initial} .

At normal ICP, both the diameter and volume flow rate for the two cases of different exponents operate within a physiological range. The diameter and volume flow rate for typical Murray's law are only slightly higher than those for the modified Murray's law (Fig. 6B,C). However, at elevated ICP, the differences for the two different exponent cases become substantial. Both the diameter and volume flow rate increase for both exponent cases (Fig. 6B and C), but the model with modified Murray's law ($n = 1.45$, blue curve) shows only a small increase in diameter which spans a range of about 100 to 170 μm . On the other hand, the model with normal Murray's law ($n = 3$, orange curve) exhibits large amplitude fluctuations, ranging from about 110 to 330 μm . Physiologically, such a large peak diameter and range in diameter is unrealistic and could likely lead to vessel rupture when ICP increases. The volume flow rate also increases with the elevated ICP, as expected when the upstream pressure exceeds the downstream pressure. However, the model with the modified Murray's law ($n = 1.45$, blue curve) shows a gradual increase in volume flow rate, while the model with normal Murray's law ($n = 3$, orange curve) exhibits an extreme increase. Excessive outflow due to elevated ICP would likely have deleterious effects. These results suggest that lymphatic capillaries that absorb the CSF in the SAS likely do not follow normal Murray's law but may instead adhere to a modified version with a smaller exponent ($n < 3$) so that the associated increase

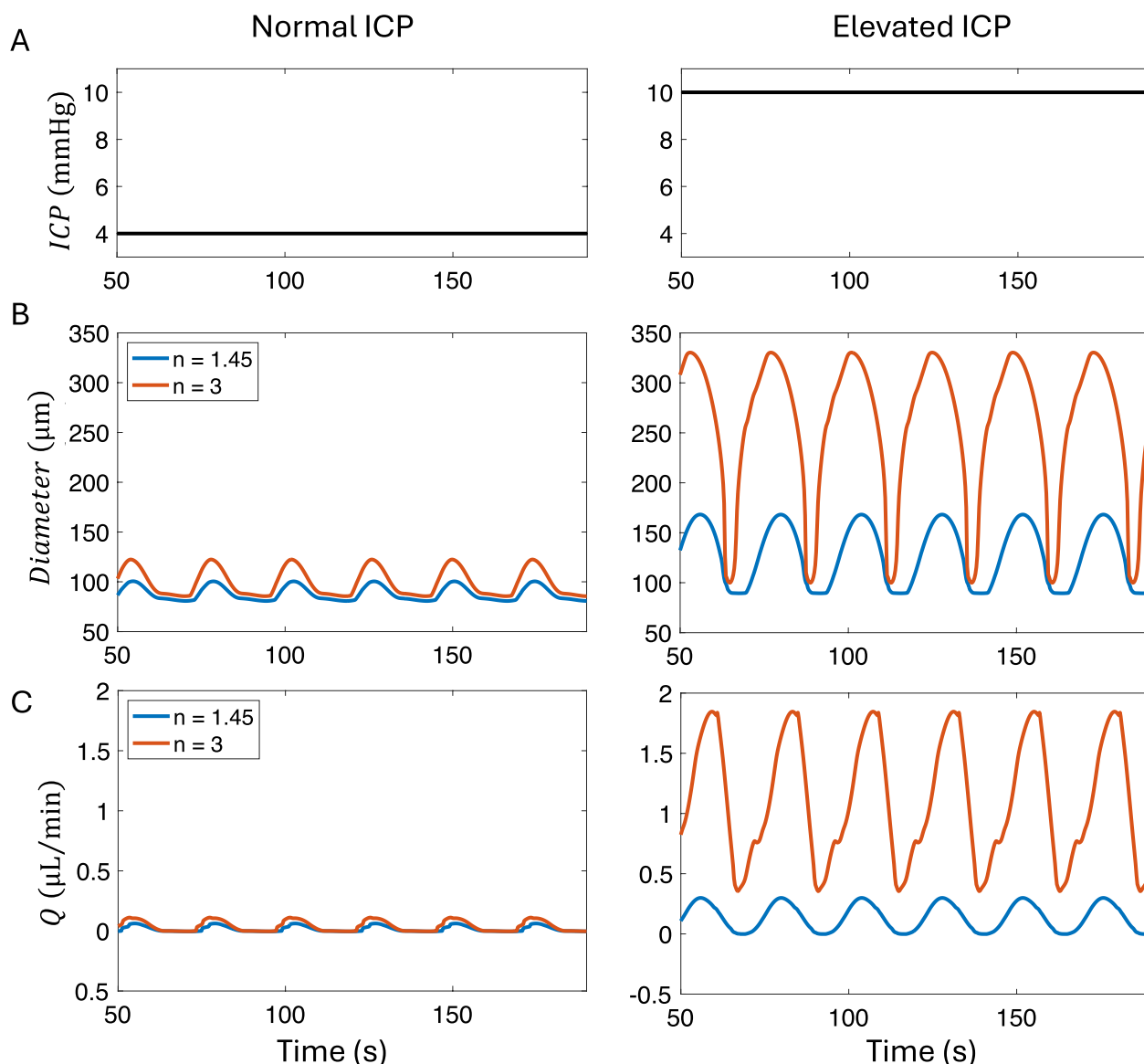


Fig. 6 Impact of lymphatic capillary branching on diameter and volume flow rate under different ICP conditions. **A** Plots of inlet pressure (ICP) for a normal (left) and elevated (right) case. **B** CLV diameter versus time for different ICP. The exponent in Murray’s law is $n = 1.45$ (blue curve) or $n = 3$ (orange curve). **C** Volume flow rate versus time for different ICP. Note that the value $n = 1.45$ comes from an experimental study of murine dermal lymphatic capillaries [39]

in hydraulic resistance will buffer transport rates with respect to changes in ICP.

Discussion

Lymphatic vessels transport fluid against an adverse pressure gradient, and CLVs are no exception. In fact, CLVs must overcome a higher adverse pressure gradient compared to other lymphatics [46, 47], which is a consequence of their anatomy which bridges the skull and cervical lymph nodes. Our numerical model suggests that both active and passive properties of the vessel wall

and the hydraulic resistance of the valve in its closed state are crucial for maintaining the vessel’s diameter and volume flow rate. Increases in outflow could be achieved by increasing active tension or perhaps decreasing vessel wall stiffness, although the latter may be difficult to achieve in practice due to its complex material composition [52]. Strategies aimed at enhancing vessel wall compliance in response to smooth muscle cell activity may improve outflow through the CLVs. We found that transport is sensitive to maximum valve resistance ($R_{V_{max}}$) when that value is small (Fig. 3C). This sensitivity results

because, if the valves do not close completely (i.e., $R_{V_{max}}$ is relatively small), substantial backflow will occur leading to a diminished net volume flow rate. Recent in vivo measurements of CLV flow in mice [12, 53] support the conclusions drawn here regarding the most sensitive parameters. Our simulations predict volume flow rates through a single CLV that range from about 0 to 0.03 $\mu\text{L}/\text{min}$ as active tension or contraction frequency are varied (Fig. 5A-B), which is qualitatively in good agreement with CLV volume flow rates reported by Du et al. [53]. They found that volume flow rates decrease from 0.071 to 0.017 $\mu\text{L}/\text{min}$ for 2-month-old versus 22-month-old mice [53]. Furthermore, they attributed this reduced transport primarily to a decrease in contraction frequency, as well as valve dysfunction that increased retrograde flow, reducing net transport.

As a lymphangion expands, the pressure inside it decreases, allowing cerebrospinal fluid (CSF) to enter. As it contracts, the CSF is transported to the next lymphangion, opening the valve in between and eventually draining to the central venous blood. It is noteworthy that the average diameters of each of the five lymphangions we model increase as one moves in the downstream direction. This is because the same parameters were used for all five lymphangions and the transmural pressure difference increases along the streamwise direction. Parameters that control the passive properties of the wall, such as distensibility (D_d) and the pressure at which the vessel is fully distended (P_d), can be modeled to increase along the downstream direction [28, 40] in order to maintain the same average diameters. Our results highlight differences between CLVs and mesenteric lymphatic vessels, in that CLVs exhibit a stronger sensitivity to wall stiffening (D_d and P_d) with changes in diameter at both positive and negative transmural pressures [28]. Due to this stiffer wall, the smooth muscle cells need to generate stronger active tension (M) to transport CSF.

In the study by Hussain et al. it was observed that the CSF outflow through CLVs decreases following TBI [12]. This study also found that the level of norepinephrine increased after TBI, which was associated with a decrease in the contraction amplitude and alteration to the frequency of the CLVs. Our simulations support the idea that decreased contraction amplitude and/or frequency lead to a decreased volume flow rate. This suggests that enhancing lymphatic activity may provide an effective target for restoring CSF drainage and enhancing brain waste clearance, as recently demonstrated by Du et al. [53]. Currently, our model only includes intrinsic pumping, which captures net volume flow rates that are in good agreement with experimental measurements. However, future numerical and/or experimental work may investigate the role of external pressures, such as

those exerted by skeletal muscles or arising from neck massage, which may enhance drainage.

Various external forces act on the CLVs from sources such as pulsatility of nearby arteries, movement due to respiration, and skeletal muscle contractions; however, results from Du et al. suggest cardiac pulsatility and respiration do not play an important role in CLV transport [53]. The pressure gradient formed by the difference between the external pressure and the intraluminal pressure affects the contractility of the CLVs. A small external pressure leads to inflation of the vessel with small amplitude contractions, while a large external pressure decreases the vessel diameter but increases the contraction amplitude. This indicates that an optimal range of external pressure likely exists, which is necessary for effective pumping and net transport. Currently, we have tested external pressure in the range of 2 mmHg to 4 mmHg. We expect that beyond about 4 mmHg, total collapse of the vessel is likely because the transmural pressure gradient will become negative. This negative pressure gradient leads to deformation of the vessel wall. However, when we tested pressures beyond 4 mmHg, numerical instability and failure occurred due to the calculation of negative diameter values. It may be helpful to test the effect of external pressure using a different model of the transmural pressure equation 6 in the future. We employed a relatively simple equation to model the transmural pressure, which we adopted from Bertram et al. due to its minimal number of parameters [28]. To accurately capture the dynamics of transmural pressure in CLVs, in vitro testing of isolated lymphangions in CLVs would be ideal for quantifying how the transmural pressure changes in response to volume loop analysis [54].

The ICP, which was assumed as the inlet pressure in our model, can increase due to gross swelling or intracranial bleeding after TBI [55]. One may hypothesize that this increased ICP could lead to rapid drainage of CSF from the skull. However, our simulations indicate that if the initial lymphatics that absorb the CSF bifurcate according to a modified version of Murray's law (with exponent substantially less than the typical $n = 3$), the associated increase in hydraulic resistance will act as a buffer that inhibits rapid CSF drainage. Murray's law, with an exponent of 3, was formulated to describe the bifurcations of arteries, aiming to explain how arterial branching minimizes hydraulic resistance. Our simulations suggest that minimizing hydraulic resistance in the initial lymphatic branches connecting the skull and CLVs is perhaps deleterious. Additionally, it is worth noting that the assumptions associated with Murray's law are already violated due to the presence of the valves, suggesting one should not expect to observe an exponent of $n = 3$ associated with the branching. Future experiments could test for

evidence of this safety mechanism by directly measuring the diameters of sequential initial lymphatic vessels or even by counting the number of branching generations. Our calculations suggest that approximately 11 versus 5 generations exist for Murray's law exponents of $n = 3$ versus $n = 1.45$. We also highlight that the exponent value $n = 1.45$ comes from a study of murine dermal lymphatic capillaries [39], and the true value for nasal lymphatics may differ substantially.

It is crucial to highlight that the large oscillations in diameters and volume flow rates seen in our elevated ICP results (Fig. 6) are highly unrealistic. During tests with different Murray's law exponents, we maintained an outlet pressure of 6 mmHg and an external pressure of 3.75 mmHg (Table 1). The inlet pressure was tested under normal ICP (4 mmHg) and elevated ICP (10 mmHg). When the inlet pressure exceeds the outlet pressure, the lymphangion loses its pumping ability and acts as a conduit, with bileaflet valves remaining open, allowing continuous flow [56, 57]. Additionally, high pressures could induce myogenic constriction, narrowing the lymphatic vessels [58]. Therefore, the exaggerated oscillations in elevated ICP conditions from our results are unrealistic. Future improvements to the transmural pressure equation, particularly focusing on the active pumping term (the second term on the right-hand side of equation (6)), should incorporate both pumping ($\Delta P < 0$) and conduit ($\Delta P > 0$) mechanisms. However, our hypothesis that nasal lymphatic capillaries may possess increased hydraulic resistance to reduce sensitivity to pressure changes could still be valid even when the vessel functions as a conduit.

Substantial evidence indicates that CSF drains through the cribriform plate to nasal lymphatics in rodents [13]. However, this pathway appears less important in humans [59], highlighting critical differences that may exist in CSF pathways for rodents versus humans. Meningeal lymphatics may potentially serve as a primary efflux route in humans. In our model, the initial lymphatic vessels are currently based on the nasopharyngeal lymphatic vessels of rodents. However, our model can be adapted to capture efflux to any other lymphatic vessels with different dimensions and properties, including meningeal lymphatic vessels.

In the recent study by Yoon et al., a complex network of lymphatics draining CSF through the nasopharynx to the cervical lymph nodes was identified [60]. This plexus contains tiny lymphatic vasculature at upstream locations, which merge into larger vessels. These larger vessels are considered pre-collector lymphatic vessels due to the presence of valves and somewhat loose covering of smooth muscle cells. Currently, our model does not include pre-collector lymphatic vessels. Future studies

could incorporate a model of the nasopharyngeal plexus and test its hydraulic resistance, which may further buffer changes in ICP. Additionally, the presence of valves in the plexus supports the idea that hydraulic resistance of the valve in its closed state is critical for CLVs when the pressure difference is high. Although the closure of lymphatic valves is not perfect and does allow a small amount of backflow, the series of valves located in the plexus likely help reduce backflow, allowing the CLVs to maintain an optimal diameter and volume flow rate.

Several important limitations of this study should be acknowledged. Spatial resolution is limited in our simulation which prevents, for example, detailed simulation of variation in contraction amplitude along the length of each lymphangion. As a consequence of using lumped parameter modeling, our predictions only include volume flow rates and pressures for three points per lymphangion (one at the center and one very close to each valve). However, a more detailed treatment is precluded by the current scarcity of quantitative data characterizing CLV geometry and physical properties. A further limitation is that the lumped parameter approach assumes that contractions of adjacent lymphangions occur with some fixed temporal phase (parameter t_d in Table 1). A more detailed analysis of relation between flow and contraction timings, including both the frequency and t_d , will be conducted in future work. In vitro observations of CLV contractions following exposure to norepinephrine reveal loss of contraction entrainment [12], which cannot be readily modeled using the lumped parameter approach. Nonetheless, the lumped parameter method is appealing in that simulations are fast and our Monte Carlo approach could be conducted efficiently. Overall, our study has uncovered valuable insights into not only fundamentals of the physical properties of CLVs, but also potential therapeutic strategies.

Conclusions

In this study, we performed simulations of CSF efflux to cervical lymphatic vessels using a lumped parameter model. This model captures the CSF drainage from the subarachnoid space, absorbed by the initial lymphatics embedded in the nasal region, which merge over several generations and drain to the cervical lymphatic vessels, eventually reaching the central venous blood. We identified parameters that are unknown and difficult to experimentally measure using a Monte Carlo search in which we matched simulation predictions to in vivo measurements. Simultaneously, we explored how the unknown parameters in the governing equations affect the median diameter of the vessels and the mean volume flow rate, concluding that magnitude of active tension, passive properties of the vessel wall, and hydraulic resistance of

the valve in its closed state have the greatest effect. We also demonstrated that increasing the active tension and/or the contraction frequency changes the overall volume flow rate, and we tested how the bifurcations of the upstream lymphatic capillaries affect the overall flow in response to elevated ICP. Narrower and longer branches (arising from a modified form of Murray’s law with exponent 1.45 [39]) increases the net hydraulic resistance, increasing the robustness of the system to elevated ICP.

This is the first numerical study of CSF drainage through CLVs. We anticipate that our rigorous parameter analysis using our proposed model will help guide future numerical studies aimed at modeling CLVs under physiological and pathological conditions. Additionally, our results form a foundation for future experiments in this field, contributing to our understanding of CSF drainage and its potential therapeutic applications.

Appendix

Derivation of lumped parameter equations

In this appendix, we present the derivation of lumped parameter fluid flow equations that are implemented as our governing equations. The equations for transmural pressure (Eq. 6) and valve resistance (Eq. 4) are directly adopted from the previous works of Bertram et al. [28, 40]. Therefore, the derivations of those equations are not included here. The mass conservation for 1D flow can be written as:

$$\frac{dA}{dt} + \frac{dQ}{dz} = 0 \tag{7}$$

where $A(z, t)$ is the cross-sectional area of the vessel and $Q(z, t)$ is the volume flow rate. Equation (7) can be integrated over one lymphangion of length $z_2 - z_1 = L$:

$$\int_{z_1}^{z_2} \left(\frac{\delta A}{\delta t} + \frac{\delta Q}{\delta z} \right) dz = 0.$$

This integration can be split into two parts:

$$\int_{z_1}^{z_2} \frac{\delta A}{\delta t} dz + \int_{z_1}^{z_2} \frac{\delta Q}{\delta z} dz = 0.$$

The first part can be computed as:

$$\int_{z_1}^{z_2} \frac{\delta A}{\delta t} dz = \frac{\delta}{\delta t} \int_{z_1}^{z_2} A dz = \frac{\delta}{\delta t} V$$

where $V(t)$ is the lymphangion volume. The second part can be computed as:

$$\int_{z_1}^{z_2} \frac{\delta Q}{\delta z} dz = Q(z_2, t) - Q(z_1, t).$$

If we denote $Q_{j+1} = Q(z_2, t)$ and $Q_j = Q(z_1, t)$, where j indexes the valves separating each lymphangion, then the equation can be rewritten in the form:

$$\frac{dV}{dt} = Q_j - Q_{j+1}. \tag{8}$$

If we assume the lymphangion has a circular cross-sectional area over a length L , then the volume V can be written as $V = \frac{1}{4}\pi D^2 L$. The temporal derivative of V is then $\frac{dV}{dt} = \frac{1}{2}\pi DL \frac{dD}{dt}$. Thus, the lumped parameter mass conservation Eq. (8) can be written in the form given by Eq. (2) in the main text:

$$\frac{dD}{dt} = \frac{2(Q_j - Q_{j+1})}{\pi LD_j}.$$

The conservation of momentum equation can be written as follows, with the assumptions that the flow is quasi-steady and laminar, the velocity in the radial direction is zero ($v_r = 0$), the axial velocity is independent of the circumferential direction ($\frac{\delta v_z}{\delta \theta} = 0$), and the pressure gradient is constant over the length of a given lymphangion ($\frac{\delta P}{\delta z} = \frac{\Delta P}{L}$):

$$\mu \left(\frac{1}{r} \frac{d}{dr} \left(r \frac{dv_z}{dr} \right) \right) = \frac{\Delta P}{L}.$$

After integrating with respect to r and applying the boundary conditions (v_z is finite at $r = 0$ and $v_z = 0$ at $r = \frac{D}{2}$), the equation can be written as:

$$v_z(z, t) = \frac{\Delta P}{4\mu L} \left(r^2 - \frac{1}{4} D(z, t)^2 \right) \tag{9}$$

where μ is the dynamic viscosity of the fluid. The volume flow rate, Q , is the integral of the axial velocity over the cross-sectional area of the pipe:

$$Q = \int_0^{2\pi} \int_0^{D/2} \frac{\Delta P}{4\mu L} \left(r^2 - \frac{1}{4} D(z, t)^2 \right) r dr d\theta.$$

After integration, we obtain the Hagen-Poiseuille equation:

$$Q = \frac{\pi D^4 \Delta P}{128 \mu L}. \tag{10}$$

Since the midpoint pressure inside a lymphangion ($P_{j,m}$) is used to calculate the pressure drop, $L/2$ should be used instead of L . Thus, Eq. (3) in the main text is obtained:

$$\frac{P_{j,1} - P_{j,m}}{L} = \frac{64\mu Q_j}{\pi D_j^4}, \quad \frac{P_{j,m} - P_{j,2}}{L} = \frac{64\mu Q_{j+1}}{\pi D_j^4}.$$

Supplementary Information

The online version contains supplementary material available at <https://doi.org/10.1186/s12987-024-00605-w>.

Supplementary Material 1.

Supplementary Material 2.

Supplementary Material 3.

Acknowledgements

Not applicable.

Author contributions

Conceptualization: DK, JT; Methodology: DK, JT; Formal analysis and investigation: DK; Writing - original draft preparation: DK; Writing - review and editing: JT; Funding acquisition: JT; Resources: JT; Supervision: JT

Funding

This work is supported by a Career Award at the Scientific Interface from Burroughs Wellcome Fund and the Research & Innovation Office at University of Minnesota.

Availability of data and materials

Data and materials are available from the authors following any reasonable request. Simulation codes are included as supplementary material.

Declarations

Ethics approval and consent to participate

Not applicable.

Consent for publication

Not applicable.

Competing interests

The authors declare no competing interests.

Received: 27 March 2024 Accepted: 2 December 2024

Published online: 19 December 2024

References

- Spector R, Snodgrass SR, Johanson CE. A balanced view of the cerebrospinal fluid composition and functions: focus on adult humans. *Exp Neurol*. 2015;273:57–68.
- Veening JG, Barendregt HP. The regulation of brain states by neuroactive substances distributed via the cerebrospinal fluid; a review. *Cerebrospinal Fluid Res*. 2010;7(1):1–16.
- Hladky SB, Barrand MA. The glymphatic hypothesis: the theory and the evidence. *Fluids Barriers CNS*. 2022;19(1):9.
- Louveau A, Plog BA, Antila S, Alitalo K, Nedergaard M, Kipnis J, et al. Understanding the functions and relationships of the glymphatic system and meningeal lymphatics. *J Clin Invest*. 2017;127(9):3210–9.
- Simon MJ, Iliff JJ. Regulation of cerebrospinal fluid (CSF) flow in neurodegenerative, neurovascular and neuroinflammatory disease. *BBA-Mol Basis Dis*. 2016;1862(3):442–51.
- Bradbury M, Cole D. The role of the lymphatic system in drainage of cerebrospinal fluid and aqueous humour. *J Physiol*. 1980;299(1):353–65.
- Brinker T, Lüdemann W, Rautenfeld D, Samii M. Dynamic properties of lymphatic pathways for the absorption of cerebrospinal fluid. *Acta Neuropathol*. 1997;94:493–8.
- Cserr HF, Harling-Berg CJ, Knopf PM. Drainage of brain extracellular fluid into blood and deep cervical lymph and its immunological significance. *Brain Pathol*. 1992;2(4):269–76.
- Walter BA, Valera V, Takahashi S, Ushiki T. The olfactory route for cerebrospinal fluid drainage into the peripheral lymphatic system. *Neuropath Appl Neuro*. 2006;32(4):388–96.
- Ma Q, Ineichen BV, Detmar M, Proulx ST. Outflow of cerebrospinal fluid is predominantly through lymphatic vessels and is reduced in aged mice. *Nat Commun*. 2017;8(1):1434.
- Ahn JH, Cho H, Kim J-H, Kim SH, Ham J-S, Park I, Suh SH, Hong SP, Song J-H, Hong Y-K, et al. Meningeal lymphatic vessels at the skull base drain cerebrospinal fluid. *Nature*. 2019;572(7767):62–6.
- Hussain R, Tithof J, Wang W, Cheetham-West A, Song W, Peng W, Sigurdson B, Kim D, Sun Q, Peng S, et al. Potentiating glymphatic drainage minimizes post-traumatic cerebral oedema. *Nature*. 2023;623(7989):992–1000.
- Proulx ST. Cerebrospinal fluid outflow: a review of the historical and contemporary evidence for arachnoid villi, perineural routes, and dural lymphatics. *Cell Mole Life Sci*. 2021;78(6):2429–57. <https://doi.org/10.1007/s00018-020-03706-5>.
- Johnston M, Zakharov A, Papaiconomou C, Salmasi G, Armstrong D. Evidence of connections between cerebrospinal fluid and nasal lymphatic vessels in humans, non-human primates and other mammalian species. *Cerebrospinal Fluid Res*. 2004;1:1–13.
- Goodman JR, Adham ZO, Woltjer RL, Lund AW, Iliff JJ. Characterization of dural sinus-associated lymphatic vasculature in human Alzheimer's dementia subjects. *Brain Behav Immun*. 2018;73:34–40.
- Norwood JN, Zhang Q, Card D, Craine A, Ryan TM, Drew PJ. Anatomical basis and physiological role of cerebrospinal fluid transport through the murine cribriform plate. *eLife*. 2019;8:44278. <https://doi.org/10.7554/eLife.44278>.
- Decker Y, Krämer J, Xin L, Müller A, Scheller A, Fassbender K, Proulx ST. Magnetic resonance imaging of cerebrospinal fluid outflow after low-rate lateral ventricle infusion in mice. *JCI Insight*. 2022;7(3).
- Spera I, Cousin N, Ries M, Kedracka A, Castillo A, Aleandri S, Vladymyrov M, Mapunda JA, Engelhardt B, Luciani P, et al. Open pathways for cerebrospinal fluid outflow at the cribriform plate along the olfactory nerves. *EBioMedicine*. 2023;91.
- Olsson B, Lautner R, Andreasson U, Öhrfelt A, Portelius E, Bjerke M, Hölttä M, Rosén C, Olsson C, Strobel G, et al. CSF and blood biomarkers for the diagnosis of Alzheimer's disease: a systematic review and meta-analysis. *Lancet Neurol*. 2016;15(7):673–84.
- Engelhardt B, Carare RO, Bechmann I, Flügel A, Laman JD, Weller RO. Vascular, glial, and lymphatic immune gateways of the central nervous system. *Acta Neuropathol*. 2016;132:317–38.
- Bolte AC, Dutta AB, Hurt ME, Smirnov I, Kovacs MA, McKee CA, Ennerfelt HE, Shapiro D, Nguyen BH, Frost EL, et al. Meningeal lymphatic dysfunction exacerbates traumatic brain injury pathogenesis. *Nat Commun*. 2020;11(1):4524.
- Plog BA, Dashnaw ML, Hitomi E, Peng W, Liao Y, Lou N, Deane R, Nedergaard M. Biomarkers of traumatic injury are transported from brain to blood via the glymphatic system. *J Neurosci*. 2015;35(2):518–26.
- Lohrberg M, Wilting J. The lymphatic vascular system of the mouse head. *Cell Tissue Res*. 2016;366(3):667–77.
- Aspelund A, Antila S, Proulx ST, Karlén TV, Karaman S, Detmar M, Wiig H, Alitalo K. A dural lymphatic vascular system that drains brain interstitial fluid and macromolecules. *J Exp Med*. 2015;212(7):991–9. <https://doi.org/10.1084/jem.20142290>.
- Xiang T, Feng D, Zhang X, Chen Y, Wang H, Liu X, Gong Z, Yuan J, Liu M, Sha Z, et al. Effects of increased intracranial pressure on cerebrospinal fluid influx, cerebral vascular hemodynamic indexes, and cerebrospinal fluid lymphatic efflux. *J Cerebr Blood F Met*. 2022;42(12):2287–302.
- Reddy NP, Krouskop TA, Newell PH Jr. A computer model of the lymphatic system. *Comput Biol Med*. 1977;7(3):181–97.
- Quick CM, Venugopal AM, Dongaonkar RM, Laine GA, Stewart RH. First-order approximation for the pressure-flow relationship of spontaneously contracting lymphangions. *Am J Physiol-Heart C*. 2008;294(5):2144–9.

28. Bertram CD, Macaskill C, Moore JE. Simulation of a chain of collapsible contracting lymphangions with progressive valve closure. *J Biomech Eng*. 2011;133(1): 011008. <https://doi.org/10.1115/1.4002799>.
29. Li H, Mei Y, Maimon N, Padera TP, Baish JW, Munn LL. The effects of valve leaflet mechanics on lymphatic pumping assessed using numerical simulations. *Sci Rep*. 2019;9(1):10649.
30. Baish JW, Kunert C, Padera TP, Munn LL. Synchronization and random triggering of lymphatic vessel contractions. *PLoS Comput Biol*. 2016;12(12):1005231.
31. Rahbar E, Moore JE Jr. A model of a radially expanding and contracting lymphangion. *J Biomech*. 2011;44(6):1001–7.
32. Elich H, Barrett A, Shankar V, Fogelson AL. Pump efficacy in a two-dimensional, fluid-structure interaction model of a chain of contracting lymphangions. *Biomech Model Mech*. 2021;20:1941–68.
33. Ballard M, Wolf KT, Nepiyushchikh Z, Dixon JB, Alexeev A. Probing the effect of morphology on lymphatic valve dynamic function. *Biomech Model Mech*. 2018;17:1343–56.
34. Wolf KT, Dixon JB, Alexeev A. Fluid pumping of peristaltic vessel fitted with elastic valves. *J Fluid Mech*. 2021;918:28.
35. Moore JE Jr, Bertram CD. Lymphatic system flows. *Annu Rev Fluid Mech*. 2018;50:459–82.
36. Hsu M, Rayasam A, Kijak JA, Choi YH, Harding JS, Marcus SA, Karpus WJ, Sandor M, Fabry Z. Neuroinflammation-induced lymphangiogenesis near the cribriform plate contributes to drainage of CNS-derived antigens and immune cells. *Nat Commun*. 2019;10(1):229. <https://doi.org/10.1038/s41467-018-08163-0>.
37. Furukawa M, Shimoda H, Kajiwara T, Kato S, Yanagisawa S. Topographic study on nerve-associated lymphatic vessels in the murine craniofacial region by immunohistochemistry and electron microscopy. *Biomed Res*. 2008;29(6):289–96.
38. Antila S, Karaman S, Nurmi H, Airavaara M, Voutilainen MH, Mathivet T, Chilov D, Li Z, Koppinen T, Park J-H, et al. Development and plasticity of meningeal lymphatic vessels. *J Exp Med*. 2017;214(12):3645–67.
39. Talkington AM, Davis RB, Datto NC, Goodwin ER, Miller LA, Caron KM. Dermal lymphatic capillaries do not obey Murray's law. *Front Cardiovasc Med*. 2022;9: 840305. <https://doi.org/10.3389/fcvm.2022.840305>.
40. Bertram CD, Macaskill C, Davis MJ, Moore JE. Development of a model of a multi-lymphangion lymphatic vessel incorporating realistic and measured parameter values. *Biomech Model Mech*. 2014;13(2):401–16. <https://doi.org/10.1007/s10237-013-0505-0>.
41. Jamalian S, Bertram CD, Richardson WJ, Moore JE. Parameter sensitivity analysis of a lumped-parameter model of a chain of lymphangions in series. *Am J Physiol-Heart C*. 2013;305(12):1709–17. <https://doi.org/10.1152/ajpheart.00403.2013>.
42. Bertram CD, Macaskill C, Moore Jr JE. Effects of lymphangion subdivision in a numerical model of a lymphatic vessel. In: Summer Bioengineering Conference, 2011:54587, 511–512. American Society of Mechanical Engineers.
43. Kim D, Gan Y, Nedergaard M, Kelley DH, Tithof J. Image analysis techniques for in vivo quantification of cerebrospinal fluid flow. *Exp Fluids*. 2023;64(11):181.
44. Tithof J, Boster KA, Bork PA, Nedergaard M, Thomas JH, Kelley DH. A network model of glymphatic flow under different experimentally-motivated parametric scenarios. *iScience*. 2022;25(5).
45. Bertram CD, Macaskill C, Davis MJ, Moore JE. Consequences of intravascular lymphatic valve properties: a study of contraction timing in a multi-lymphangion model. *Am J Physiol-Heart C*. 2016;310(7):847–60. <https://doi.org/10.1152/ajpheart.00669.2015>.
46. Yang B, Zador Z, Verkman A. Glial cell aquaporin-4 overexpression in transgenic mice accelerates cytotoxic brain swelling. *J Biol Chem*. 2008;283(22):15280–6.
47. Moazen M, Alazmani A, Rafferty K, Liu Z-J, Gustafson J, Cunningham ML, Fagan MJ, Herring SW. Intracranial pressure changes during mouse development. *J Biomech*. 2016;49(1):123–6.
48. Xie C, Wei W, Zhang T, Dirsch O, Dahmen U. Monitoring of systemic and hepatic hemodynamic parameters in mice. *JoVE-J Vis Exp*. (92), 2014:51955.
49. Bertram CD, Macaskill C, Davis MJ, Moore JE. Contraction of collecting lymphatics: organization of pressure-dependent rate for multiple lymphangions. *Biomech Model Mech*. 2018;17(5):1513–32. <https://doi.org/10.1007/s10237-018-1042-7>.
50. Harris CR, Millman KJ, Walt SJ, Gommers R, Virtanen P, Cournapeau D, Wieser E, Taylor J, Berg S, Smith NJ, Kern R, Picus M, Hoyer S, Kerkwijk MH, Brett M, Haldane A, Río JF, Wiebe M, Peterson P, Gérard-Marchant P, Sheppard K, Reddy T, Weckesser W, Abbasi H, Gohlke C, Oliphant TE. Array programming with NumPy. *Nature*. 2020;585(7825):357–62. <https://doi.org/10.1038/s41586-020-2649-2>.
51. Virtanen P, Gommers R, Oliphant TE, Haberland M, Reddy T, Cournapeau D, Burovski E, Peterson P, Weckesser W, Bright J, van der Walt SJ, Brett M, Wilson J, Millman KJ, Mayorov N, Nelson ARJ, Jones E, Kern R, Larson E, Carey CJ, Polat İ, Feng Y, Moore EW, VanderPlas J, Laxalde D, Perktold J, Cimrman R, Henriksen I, Quintero EA, Harris CR, Archibald AM, Ribeiro AH, Pedregosa F, van Mulbregt P. SciPy 1.0 Contributors: SciPy 1.0: Fundamental Algorithms for Scientific Computing in Python. *Nat Methods*. 2020;17:261–72. <https://doi.org/10.1038/s41592-019-0686-2>.
52. Breslin JW, Yang Y, Scallan JP, Sweat RS, Adderley SP, Murfee WL. Lymphatic vessel network structure and physiology. *Compr Physiol*. 2018;9(1):207.
53. Du T, Raghunandan A, Mestre H, Plá V, Liu G, Ladrón-de-Guevara A, Newbold E, Tobin P, Gahn-Martinez D, Pattanayak S, Huang Q, Peng W, Nedergaard M, Kelley DH. Restoration of cervical lymphatic vessel function in aging rescues cerebrospinal fluid drainage. *Nat Aging*. 2024. <https://doi.org/10.1038/s43587-024-00691-3>.
54. Davis MJ, Rahbar E, Gashev AA, Zawieja DC, Moore JE Jr. Determinants of valve gating in collecting lymphatic vessels from rat mesentery. *Am J Physiol-Heart C*. 2011;301(1):48–60.
55. Dunn LT. Raised intracranial pressure. *J Neurol Neurosurg Ps*. 2002;73(suppl 1):23–7.
56. Scallan JP, Zawieja SD, Castorena-Gonzalez JA, Davis MJ. Lymphatic pumping: mechanics, mechanisms and malfunction. *J Physiol*. 2016;594(20):5749–68.
57. Quick CM, Venugopal AM, Gashev AA, Zawieja DC, Stewart RH. Intrinsic pump-conduit behavior of lymphangions. *Am J Physiol-Reg I*. 2007;292(4):1510–8.
58. Davis MJ, Davis AM, Ku CW, Gashev AA. Myogenic constriction and dilation of isolated lymphatic vessels. *Am J Physiol-Heart C*. 2009;296(2):293–302.
59. Ringstad G, Eide PK. Glymphatic-lymphatic coupling: assessment of the evidence from magnetic resonance imaging of humans. *Cell Mol Life Sci*. 2024;81(1):1–14.
60. Yoon J-H, Jin H, Kim HJ, Hong SP, Yang MJ, Ahn JH, Kim Y-C, Seo J, Lee Y, McDonald DM, et al. Nasopharyngeal lymphatic plexus is a hub for cerebrospinal fluid drainage. *Nature*. 2024;1–10.

Publisher's Note

Springer Nature remains neutral with regard to jurisdictional claims in published maps and institutional affiliations.